

Synergistic Effect of Ni and Co Alloying on Corrosion Behavior of Fe(Ni,Co)P₁₃C₇ Metallic Glasses in 1M NaCl Solution

B. Sarac

Erich Schmid Institute of Materials Science, Austrian Academy of Sciences, 8700 Leoben, Austria.

+43(0)3842-804-101

E-mail: baran.sarac@oeaw.ac.at

Received: 10 September 2021 / Accepted: 25 October 2021 / Published: 10 November 2021

This study focuses on the transition metal and metalloid containing advanced amorphous alloys possessing excellent corrosion resistance in 1 M NaCl solution. 4 different alloy compositions, including base composition and with Ni and/or Co additions, Fe_{80-x-y}Ni_xCo_yP₁₃C₇, are investigated for their electrical characteristics by electrochemical impedance spectroscopy (EIS) and corrosion behavior by linear sweep voltammetry. A prolonged characteristic frequency in the Bode phase due to double peak formation and the steepest increase in the near-DC region is observed for the Fe₆₀Ni₁₀Co₁₀P₁₃C₇. From the fitting of the EIS data with R(QR(QR)) circuit model, the lowest capacitance ($3.87 \times 10^{-5} \text{ S s cm}^{-2}$) and largest resistance ($3390 \text{ } \Omega \text{ cm}^{-2}$) are obtained for the same alloy, confirming the highest passivity. Low anodic Tafel slope (23 mV dec^{-1}) and corrosion current density ($5 \text{ } \mu\text{A cm}^{-2}$) yield a minimal annual corrosion rate of 0.08 mm yr^{-1} . Hence, this multi-component metallic glass alloy is foreseen to replace other relevant metals due to its enhanced corrosion resistance in a saline environment and cost-effective material and production costs.

Keywords: metallic glass, transition elements, electrochemical impedance spectroscopy, polarization curve, corrosion properties

1. INTRODUCTION

In polycrystalline materials, the grain size and shape, number and distribution of phases, and structure of the grain boundaries define the electrochemical performance (1-7). With the absence of grain boundaries and defects, the amorphous monolithic glasses show pronounced corrosion resistance in a variety of environments and time scales (8-16). Among metallic glass (MG) types, because of their high abundance, low material costs and significant corrosion resistance, Fe-based metallic glasses are going to play an essential role in extreme environments (17-21).

The first Fe-P-C MG foil production by Duwez and Lin dates back to 1967 (22). The first development of the $\text{Fe}_{80}\text{P}_{13}\text{C}_7$ MG alloy and its structural analysis via TOF neutron scattering was performed by Mizoguchi et al. in 1975 (23). Later on, with the inclusion of Ni, $\text{Fe}_{80-x}\text{Ni}_x\text{P}_{13}\text{C}_7$ and $\text{Fe}_{72-x}\text{Ni}_x\text{P}_{13}\text{C}_7$ compositions in 1 mm diameter were reported to show ultra-high compressive plasticity and appealing magnetic properties (24). Following this, our group has examined the multiscale effects in this alloy system using aberration-corrected high-resolution transmission electron microscopy and found that the homogeneously dispersed nanocrystals of several nanometers and soft/hard regions on micron-scale are the main reason for such high plasticity (up to 50%) (25). $\text{Fe}_{80-x}\text{Co}_x\text{P}_{13}\text{C}_7$ MG alloys were first introduced in 1976 by Fujimori et al. (26) as magnetically very soft materials. The first simultaneous addition of the transition elements Ni and Co at the expense of Fe ($\text{Fe}_{80-x-y}\text{Ni}_x\text{Co}_y\text{P}_{13}\text{C}_7$) in fully amorphous ribbon form and their synergistic impact on thermal, structural and magnetic properties upon annealing and/or fluxing was achieved recently by our group (27).

Although corrosion behavior of FeNi- and FeCo-based MGs in the saline medium was reported in the literature (28-35), this is a first-time study that the electrochemical properties of the Fe(Ni,Co)PC MG system with metalloid content was investigated. The morphologic, i.e. digital imaging and scanning electron microscopy (SEM)), and composition, i.e. energy-dispersive X-ray spectroscopy (EDS), analyses of the melt-spun ribbons were conducted. The electrical characteristics of the samples were assessed in 1 M NaCl solution at ambient conditions using electrochemical impedance spectroscopy (EIS) and a corresponding fit generated by an equivalent circuit model (ECM). The polarization curves obtained by linear sweep voltammetry (LSV) enabled to measure the anodic (β_a) and cathodic (β_c) Tafel slopes, corrosion current densities (j_{corr}), and corrosion potentials (E_{corr}). The annual corrosion rate (V_{acr}) calculated from the Tafel slopes and other physical parameters provide a general understanding of the influence of Ni and/or Co additions at the expense of Fe.

2. MATERIALS AND METHODS

2.1. Melt-spinning of Metallic Glass Ribbons

The master alloys were prepared out of Co, Fe, and Ni flakes (99.99% purity), FeP pre-alloy (99.5% purity) and graphite powder (99.99% purity) under high purity Ar atmosphere by induction melting (99.999% purity) using Edmund Bühler GmbH. The ingots were melted three times for homogenization. Subsequently, the ingots were heated to 1873 K and kept at this temperature for a few minutes under moderate vacuum (10^{-3} mbar). The melt-spinning was conducted under high purity Ar atmosphere with a vacuum of $\sim 5 \times 10^{-3}$ mbar. A gas pressure of 200 bar ejects the molten metal onto a rapidly rotating copper wheel. Solidification of the ribbons occurs on the melt spinning wheel with a cooling rate of 10^5 - 10^6 K s^{-1} (36). The meters-long continuous ribbons form by detaching from the copper wheel due to the difference in the thermal expansion coefficients. Hereafter, the compositions will be denoted as S1: $\text{Fe}_{80}\text{P}_{13}\text{C}_7$, S2: $\text{Fe}_{60}\text{Co}_{20}\text{P}_{13}\text{C}_7$, S3: $\text{Fe}_{60}\text{Ni}_{20}\text{P}_{13}\text{C}_7$, and S4: $\text{Fe}_{60}\text{Ni}_{10}\text{Co}_{10}\text{P}_{13}\text{C}_7$.

2.2. Scanning Electron Microscopy & Energy Dispersive X-ray & Digital Imaging

SEM imaging was performed using a Quanta FEG 250 microscope with 10 kV acceleration voltage, the working distance of 8.5 mm, and magnification of 5k \times . The sample dimension of 1.6 mm \times 5 mm was used, where the sample was cut by scissor and stuck onto the carbon pad and grounded by copper tape to enhance the image quality. Energy-dispersive X-ray analysis was implemented by Zeiss LEO 1525 scanning electron microscope (SEM) equipped with an XFlash Detector 6|60 energy-dispersive X-ray spectroscopy (EDS) unit under 20 kV at a working distance of 10 mm. Digital imaging was performed using a 12MP AF sensor camera with a pixel size of 1.4 μm and an F1.5 mode aperture. For digital imaging, the ribbons of different compositions were cut to a 4-5 cm length and placed side by side for comparison.

2.3. Electrochemical Measurements

The electrochemical measurements were implemented using a PARSTAT 4000A Potentiostat Galvanostat (Princeton Applied Research, USA). Data was obtained via VersaStudio 2.60.6 software. The ribbons were cut by scissor to a length of ~ 2 cm, where one side was coiled by copper tape (Busch 1799) to fit into the alligator clips (SKS Hirschmann KLEPS 2600) of the working electrode and to establish high electrical conductivity. The potentials in the polarization study were given with respect to Ag/AgCl reference electrode with saturated KCl solution with a redox potential of +0.197 V vs. a standard hydrogen electrode at 25 $^{\circ}\text{C}$. The counter electrode was a mirror-polished Pt wire (99.9%) of 0.8 mm diameter. 5 mL 1 M NaCl solution was dissolved in deionized water and purged with argon gas for 15 minutes to reduce down the impurities. Prior to the measurements, 15 minutes of waiting time (at 25 $^{\circ}\text{C}$ under atmospheric pressure) was applied. A new solution was used for each measurement. The electrochemical impedance spectroscopy (EIS) measurements at open circuit potential (OCP) with an amplitude of 10 mV were recorded from 1 MHz to 0.01 Hz. The EIS data simulation was performed with the electrical equivalent circuit of $R(QR(QR))$ using ZSimpWin V.3.10, where R and Q represent the resistance and constant phase element, respectively. The goodness of the fit (χ^2) lies between $1.5 - 2.5 \times 10^{-2}$ with low error for individual parameters. Following the EIS-OCP, linear sweep voltammetry (LSV) scans were recorded within the same solution from 0.25 V to -0.25 V with respect to OCP at a scan rate of 0.167 mV s^{-1} using a step height of 0.5 mV and step time of 3 s. Tafel fit function of VersaStudio 2.60.6 was used to measure the β_c and β_a , corrosion current density j_{corr} and potential E_{corr} . The equivalent weight EW of each alloy was calculated from $EW = 1 / \sum \frac{f_i n_i}{w_i}$ where f_i , n_i and w_i are mass fraction, electrons exchanged, and atomic weight, respectively, of the i^{th} alloying element. The theoretical alloy density D was calculated from the equation $\frac{1}{D} = \sum_{i=1}^n \frac{m_i}{D_i}$. Here, D_i is the density and m_i is the mass fraction of each constituent element within the alloy, where $\sum_{i=1}^n m_i = 1$. Annual corrosion rate, V_{acr} , was subsequently retrieved from the calculated EW , j_{corr} and D parameters.

3. RESULTS AND DISCUSSION

3.1. Compositional and Morphological Analysis

Table 1 shows the compositional variation between the samples upon Ni and/or Co additions. The average width and thickness values and the submerged area used in the EIS and LSV measurements are also provided. Figure 1a depicts the digital microscopy images of the produced defect- and pore-free ribbons. Surface irregularities such as bumps or scratches occur due to the irregular flow of the molten metal upon melt-spinning and the surface roughness of the spinning copper wheel (Figure 1b).

Table 1. Compositional analysis of the selected MG ribbons. S1: $\text{Fe}_{80}\text{P}_{13}\text{C}_7$, S2: $\text{Fe}_{60}\text{Co}_{20}\text{P}_{13}\text{C}_7$, S3: $\text{Fe}_{60}\text{Ni}_{20}\text{P}_{13}\text{C}_7$, and S4: $\text{Fe}_{60}\text{Ni}_{10}\text{Co}_{10}\text{P}_{13}\text{C}_7$. The composition of each component is within ± 2 at. %.

Sample No	Fe	Ni	Co	P, C, Others	Width (± 0.1 mm)	Thickness (μm)	Submerged Area (mm^2)
S1	84	–	–	16	1.55	49.7 ± 7.9	2.965
S2	65	–	22	13	1.82	72.8 ± 16.8	3.105
S3	66	21	–	13	1.71	41.7 ± 4.0	2.938
S4	65	10	11	14	1.62	41.0 ± 8.7	2.812

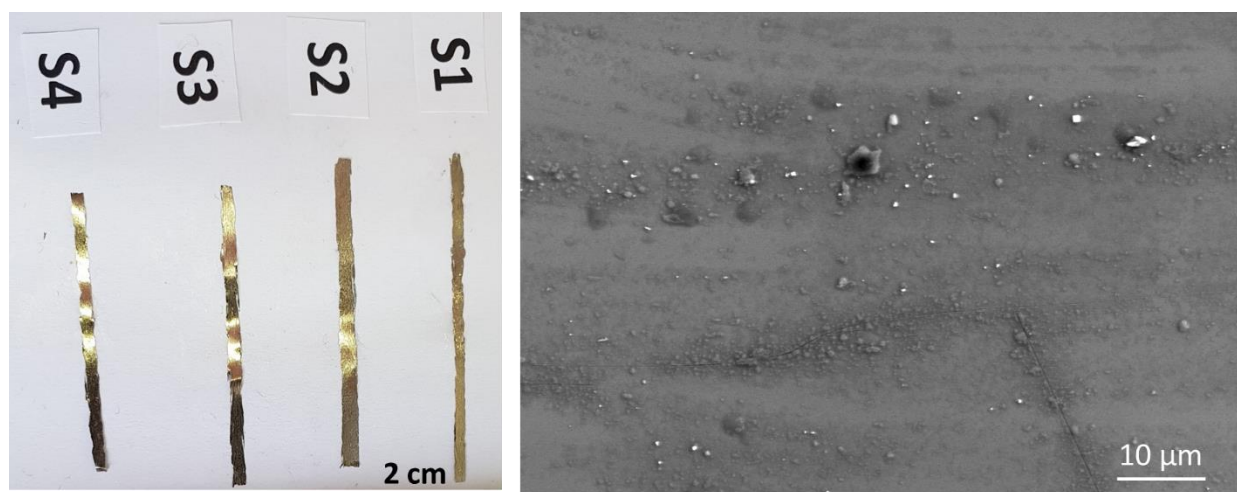


Figure 1. (a) Digital microscope imaging of 4 different ribbon compositions produced by melt spinning. (b) SEM imaging of a representative S4 sample.

3.2. Electrochemical Impedance Spectroscopy

Figure 2a shows the electrochemical impedance spectroscopy (EIS)-Nyquist plot comparison of these 4 different compositions. As it can be noticed, S1 has a quite different behavior compared to the other 3 compositions. Figure 2a inset depicts that S1 has a semicircle profile with a tail, showing a maximum at $Z_{re} = 53 \Omega \text{ cm}^2$ and $Z_{im} = 40 \Omega \text{ cm}^2$. The simulation fit (dashed line) has an acceptable

agreement with the measurement profile. With the inclusion of Ni and/or Co, the impedance becomes significantly larger. The inclusion of Ni (20 at.%) has a more significant impact on the enlarging of the plot compared to Co inclusion (20 at.%). The inclusion of Ni and Co, each 10 at%, has a synergistic effect on the further enlarging of the semicircle with impedance up to an order of $1000 \Omega \text{ cm}^2$. This finding is interesting since Fe, Ni and Co are transition metal elements with almost zero negative heat of mixing between two different atom pairs and very similar atomic size. The synergistic effect of these elements were previously determined in a variety of fields such as oxygen evolution (37-39) and hydrogen evolution (40, 41) reactions from the increase in the speed of electron transport possibly due to abundance of surface and inner active sites (e.g. free volume between atomic clusters and between atoms within the cluster) in the simultaneous Ni and Co additions upon synthesis (42). Since the capacitance is inversely related to impedance, S4 shows the most negligible capacitance (see Figure 2b and inset). The lowest and highest phase angles were attained for S1 (69.7°) and S3 (78.9°) samples at their characteristic frequencies of ~ 30 Hz (Figure 3a). S2 has a relatively larger frequency range where the Bode phase angle, φ , stays above 70° . Hence, the inclusion of Ni increases φ remarkably, whereas the increase in φ via Co addition is not as significant. On the other hand, with Ni addition a visible shift in the characteristic medium-frequency peak towards larger frequencies was observed. Sample S4's φ vs. f profile resembles that of the S2, but the synergistic effect of Ni and Co yields a dual-peak profile, the first one at 71.7° and the second one at 74.5° . This effect also enlarges the region where S4 remains above 70° (between 2.5 Hz and 1585 Hz). The Bode magnitude plots show distinct variations, particularly in the near-DC range (Figure 3b). The smallest and largest changes in slope in the mid-frequency range are observed for the S1 and S4 samples, respectively.

Table 2. ECM analysis of compositions S1-S4. R_s : solution, R_2 : charge transfer, and R_3 : passive oxide – MG interface resistance. Constant phase element parameter of Y_1 : double layer, and Y_2 : passive oxide – MG interface. Constant phase element exponential of n_1 : double layer, and n_2 : passive oxide – MG interface. χ^2 : goodness of the fit.

	S1	S2	S3	S4
$R_s/\Omega \text{ cm}^2$	0.21	0.19	0.20	0.21
$Y_1/S \text{ s}^n \text{ cm}^{-2}$	6.55×10^{-3}	4.71×10^{-4}	8.05×10^{-4}	2.3×10^{-4}
n_1	1	0.7	1	0.77
$R_1/\Omega \text{ cm}^2$	383	1.7	1090	2
$Y_2/S \text{ s}^n \text{ cm}^{-2}$	2.40×10^{-3}	7.16×10^{-5}	9.24×10^{-4}	3.87×10^{-5}
n_2	0.83	1	0.9048	1
$R_2/\Omega \text{ cm}^2$	141	2680	1400	3390
Chi squared/ χ^2	2.49×10^{-2}	2.26×10^{-2}	3.17×10^{-2}	1.53×10^{-2}

Table 2 compares the simulation data with a selected $R_s(Q_1R_1(Q_2R_2))$ circuit for 4 different compositions. Here, R_s is the solution resistance, including contact resistance between the active electrode and its interface, electrolyte resistance, and internal resistance of active electrodes (43). The measured R_s values are very small and close to each other, confirming the stability of the electrolyte and measurement setup. R_1 is the charge transfer resistance, whereas Y_1 and n_1 are the double layer

capacitance parameter and exponent, respectively, of the constant phase element Q_1 due to the ion interactions on the material surface. R_2 the passive oxide layer – metallic glass interface resistance, and Y_2 and n_2 belong to this interface's phase element constant, Q_2 .

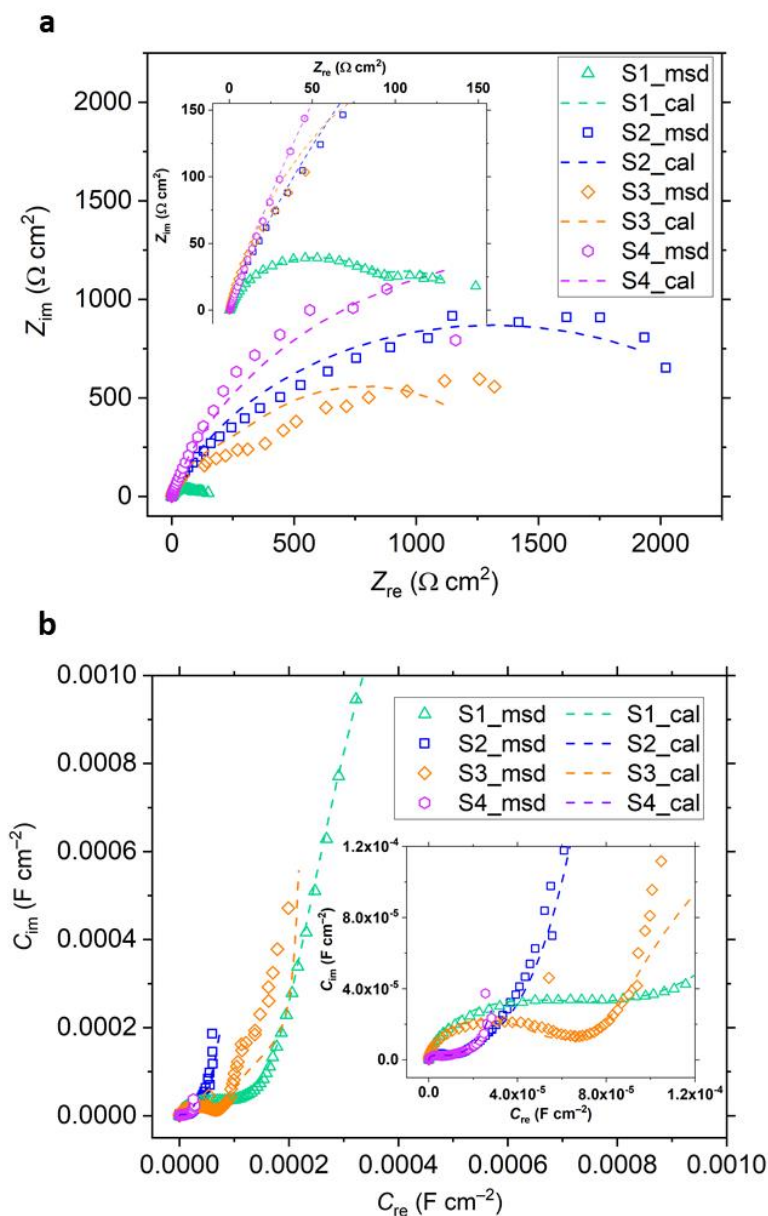


Figure 2. (a) Nyquist and (b) capacitance plots of S1-S4 measured at OCP from 1 MHz to 0.01 Hz. Z_{re} : real and Z_{im} : imaginary part of impedance. C_{re} : real and C_{im} : imaginary part of capacitance.

The highest Y_1 is attained for the S1 sample. R_1 value is lowest for S2, followed by S4, and highest for S3. Hence, the high Fe content without any Ni or Co addition has lower transport kinetics at the electrolyte-electrode interface, but on the other hand, a pronounced double-layer is formed. In contrast, a considerable resistance is obtained between the oxide layer and metallic glass ribbon (as designated by R_2), particularly for S4 and S2 samples with Co content. This passive oxide layer – metallic

glass interface has the lowest capacitance of $3.87 \times 10^{-5} \text{ S s cm}^{-2}$ (calculated from $C_2 = Y_2 \times \omega_{max}^{n_2-1}$, where ω_{max} is the characteristic frequency obtained from the peak of the semicircle in the Nyquist plot, and $n_2 = 1$ (44)) for S4, followed by S2. In a previous paper, our group has shown the existence of a natural oxide layer of several nanometers on Fe-Ni-Mo-B metallic glass microfibers produced with similar production and vacuum conditions by scanning transmission electron microscopy (45). Thus, the findings show that for the Co-containing alloys, even though an abundance of electron transfer is present and the ions can penetrate inside the oxide layer, they are blocked by this oxide layer, and thus minimum ionic diffusion and electron transfer occurs at the oxide-metallic glass interface.

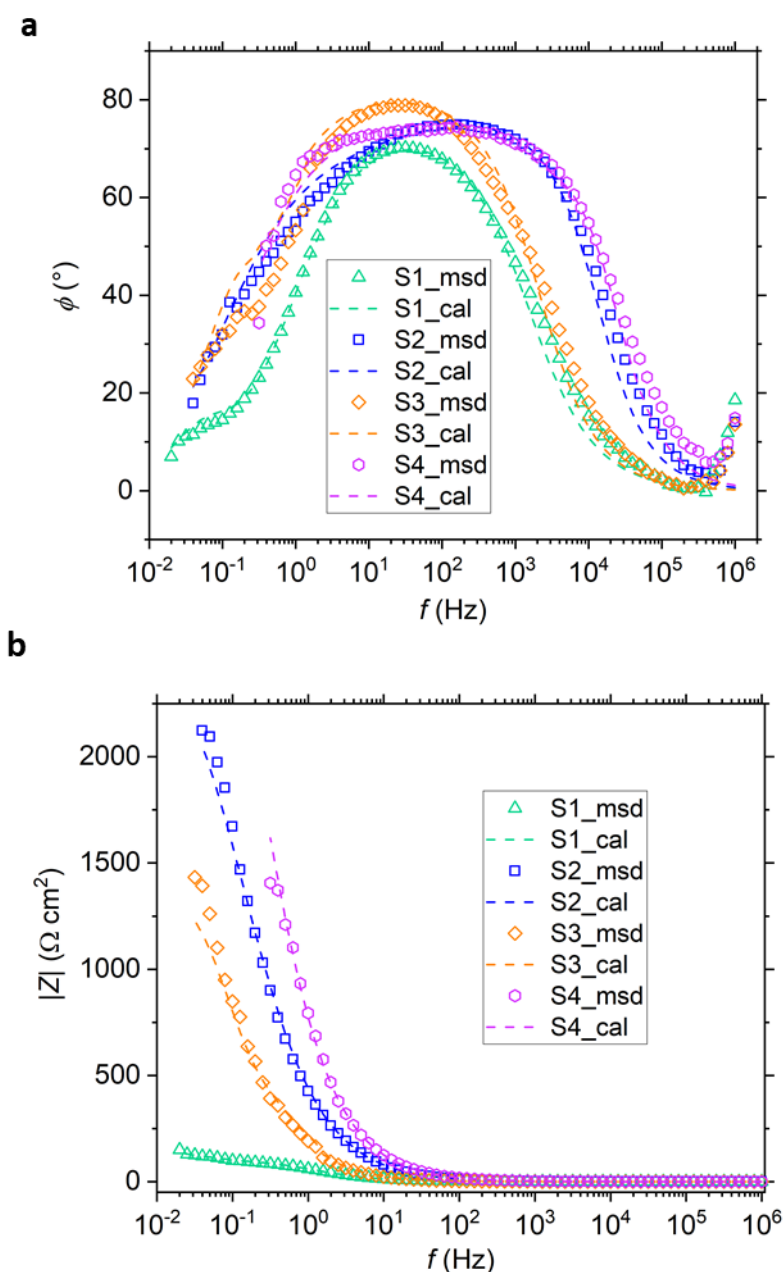


Figure 3. (a) Bode phase and (b) Bode magnitude plots of S1-S4 measured at OCP from 1 MHz to 0.01

Hz. Φ : phase angle, f : applied frequency, $|Z| = \sqrt{Z_{re}^2 + Z_{im}^2}$.

3.3. Potentiodynamic Corrosion Test

Figure 4 shows the potentiodynamic polarization behavior of 4 different types of metallic glass ribbons. By Co inclusion, pronounced shifts from negative to positive values are observed. Besides, the corrosion current density, j_{corr} , decreases to 10^{-8} A cm^{-2} level by the co-inclusion of Co and Ni at the expense of Fe.

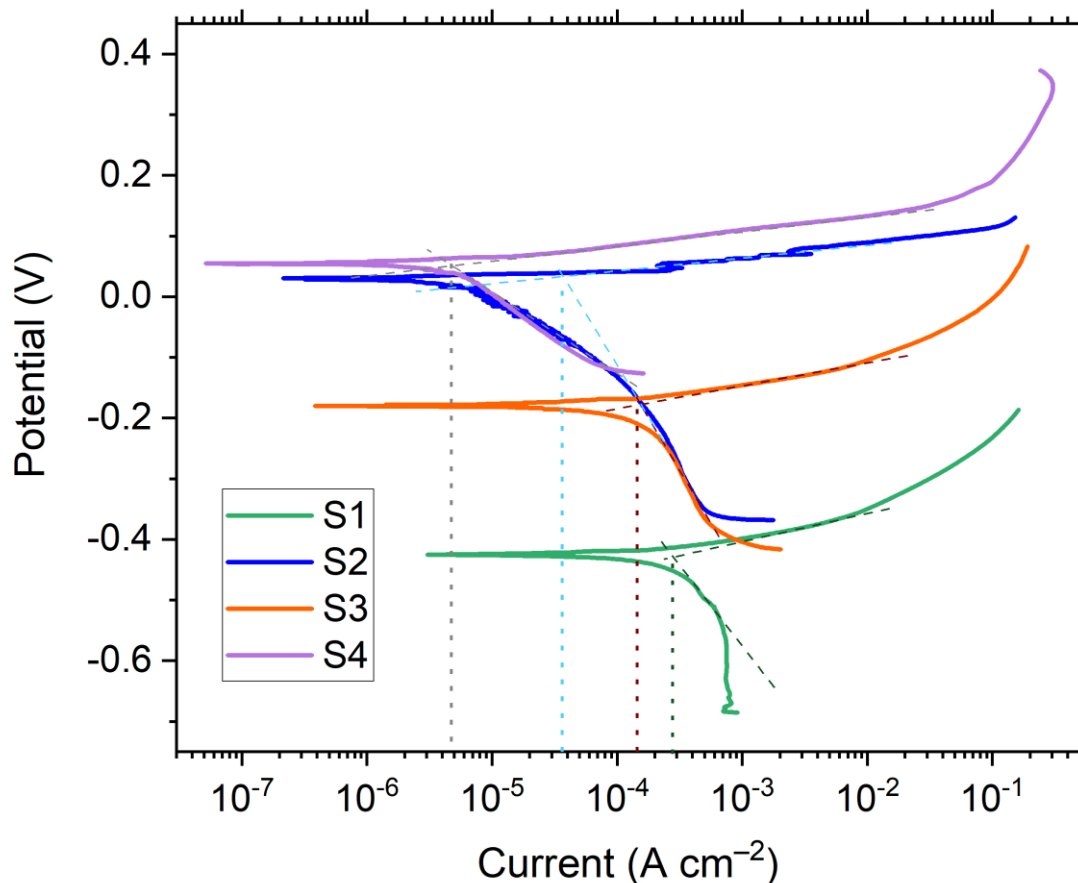


Figure 4. Potentiodynamic polarization curves of the considered alloys at a scan rate of 0.167 mV s⁻¹ vs. Ag/AgCl (KCl sat.) reference electrode. The dashed lines are the anodic and cathodic Tafel fits, whereas the dotted vertical lines indicate the intersection points of these fitting lines corresponding to corrosion current density, j_{corr} , and corrosion potential, E_{corr} .

Table 3 depicts the parameters taken from the Tafel fit measurements and materials intrinsic properties. The average corrosion rate, V_{acr} (micrometer per year, $\mu m yr^{-1}$), is calculated from eq. 1 (46):

$$V_{acr} = \frac{3.27 \times j_{corr} \times EW}{D}, \tag{1}$$

where j_{corr} has units of $\mu A cm^{-2}$, EW is the equivalent weight, and D is the theoretical density of alloy. The highest annual corrosion rate is observed for the S1 sample with no Ni and Co addition (4.8 mm yr⁻¹).

Table 3. Comparison of different HEAs. D : theoretical alloy density, EW : the equivalent weight of the alloys, β_a : anodic beta constant, β_c : cathodic beta constant, E_{corr} : corrosion potential, j_{corr} : exchange current density, V_{acr} : average corrosion rate. Errors of β_a and β_c are within ± 3 mV dec⁻¹, whereas errors of E_{corr} and j_{corr} are within ± 2 mV and ± 1 $\mu\text{A cm}^{-2}$, respectively.

Composition	D (g cm ⁻³)	EW (-)	β_a (mV dec ⁻¹)	β_c (mV dec ⁻¹)	E_{corr} (mV)	j_{corr} ($\mu\text{A cm}^{-2}$)	V_{acr} (mm yr ⁻¹)
Fe ₈₀ P ₁₃ C ₇ (S1)	6.005	30.96	43	289	-424	285	4.80
Fe ₆₀ Co ₂₀ P ₁₃ C ₇ (S2)	6.145	31.35	25	324	29	38	0.63
Fe ₆₀ Ni ₂₀ P ₁₃ C ₇ (S3)	6.149	31.32	38	360	-178	158	2.63
Fe ₆₀ Ni ₁₀ Co ₁₀ P ₁₃ C ₇ (S4)	6.147	31.34	23	158	53	5	0.08

The addition of only Ni makes a slight improvement (2.63 mm yr⁻¹), whereas only Co addition improves the corrosion resistance significantly (0.63 mm yr⁻¹). A low corrosion rate down to 0.08 mm yr⁻¹ is attained by the concomitant addition of Ni and Co. The annual corrosion rate obtained from the potentiodynamic polarization test shows that sample S4 performs better than 316L stainless steel at similar NaCl concentrations (47). Furthermore, V_{acr} of the S4 sample is comparable or smaller than calculated for different steels, i.e. immersing API X120 in 3.5 wt% NaCl solution (48), immersing API 5L X65, and other similarly micro-alloyed steels in 1-10 wt.% NaCl solution (49), or cyclic corrosion tests of YS460 MPa grade in 5 wt.% NaCl solution (50).

4. CONCLUSIONS

This study examines the influence of the Ni and/or Co inclusion as the second (and third) element on the electrochemical behavior and corrosion properties. Overall, the results indicate that the sample's resistance and capacitance can be tuned by a moderate amount of Ni and Co additions. High corrosion stability, particularly for the S4 and S2 samples, is attributed to relatively higher resistance and lower capacitance at the metal oxide – metallic glass interface, yielding a barrier towards the passage of ions into the metallic glass. An appearance of a second peak in the Bode phase graph causing the enlargement of the characteristic mid-frequency region and the steepest change in the slope towards the near-DC range in the Bode magnitude plots are observed for the S4 sample with simultaneous Co and Ni addition. Furthermore, the findings from the Tafel fitting again corroborate the synergistic effect of the simultaneous Fe and Co addition. Very small j_{corr} (5 $\mu\text{A cm}^{-2}$) and β_a (23 mV dec⁻¹) is observed for the S4 sample, where more energy is necessary for the initiation of corrosion since E_{corr} of S4 shifts towards larger potentials. The corresponding annual corrosion rate estimated for this sample is 0.08 mm yr⁻¹, outperforming many of the conventionally used steel types characterized under similar conditions. Hence, this study is expected to provide a guideline for developing and assessing novel amorphous Fe-based glasses and other Fe-containing crystalline alloys with multiple metallic elements.

ACKNOWLEDGEMENTS

The author thanks Eray Yüce for his assistance in the production of the ribbons, Selin Gümrükcü for her contribution on the electrochemical characterization. The author gratefully acknowledges the financial support by the Austrian Science Fund (FWF) under project grant I3937-N36 (PI: Baran Sarac). **ORCID ID:** 0000-0002-0130-3914

References

1. C. Keller, A. Desrues, S. Karuppiah, E. Martin, J.P. Alper, F. Boismain, C. Villevieille, N. Herlin-Boime, C. Haon, P. Chenevier, *Nanomaterials*, 11 (2021) 307.
2. S. Wu, B. Yu, Z. Wu, S. Fang, B. Shi, J. Yang, *RSC Adv.*, 8 (2018) 8544.
3. V. Afshari, C. Dehghanian, *Corros. Sci.*, 51 (2009) 1844.
4. X. Zhang, R.Q. Ma, Z.H. Wang, Z.H. Zhou, G.H. Yang, X. Cai, *Int. J. Electrochem. Sci.*, 16 (2021) 151060.
5. X.L. Wei, D.J. Zhu, W.Y. Zhu, D.L. Wu, J. Li, C. Zhang, *Int. J. Electrochem. Sci.*, 15 (2020) 4840.
6. A. Wang, W.T. Jia, C.L. Cheng, Q.C. Le, F. Yang, *Int. J. Electrochem. Sci.*, 13 (2018) 9017.
7. Y.D. Yu, L.X. Sun, H.L. Ge, G.Y. Wei, L. Jiang, *Int. J. Electrochem. Sci.*, 12 (2017) 485.
8. Y.G. Wang, Y.J. Li, S.P. Pan, B.D. Fu, J.Y. Qin, W.M. Wang, *Int. J. Electrochem. Sci.*, 11 (2016) 3512.
9. X. Li, F. Lv, Y.X. Geng, F. Qi, Y.J. Xu, F. Liu, Y.X. Wang, *Int. J. Electrochem. Sci.*, 12 (2017) 726.
10. L.S. Yu, J.L. Tang, J.C. Qiao, H. Wang, Y.Y. Wang, M. Apreutesei, M. Chamas, M. Duan, *Int. J. Electrochem. Sci.*, 12 (2017) 6506.
11. C.L. Li, C.Y. Chung, B.S. Lou, J.W. Lee, J.P. Chu, *Int. J. Electrochem. Sci.*, 12 (2017) 12074.
12. K.M. Emran, H. Al-Refai, *Int. J. Electrochem. Sci.*, 12 (2017) 6404.
13. A. Liens, B. Ter-Ovannessian, N. Courtois, D. Fabregue, T. Wada, H. Kato, J. Chevalier, *Corros. Sci.*, 177 (2020) 108854.
14. L.W. Hu, X. Liu, T.X. Chen, G.M. Le, J.F. Li, F.S. Qu, Y.Z. Zhou, L. Qi, D. Wang, *Vacuum*, 185 (2021) 109996.
15. B. Sarac, T. Karazehir, M. Micusik, C. Halkali, D. Gutnik, M. Omastova, A.S. Sarac, J. Eckert, *ACS Appl. Mater. Interfaces*, 13 (2021) 23689.
16. B. Sarac, T. Karazehir, E. Yüce, M. Mühlbacher, A.S. Sarac, J. Eckert, *Mater. Des.*, 210 (2021) 110099.
17. G. Li, Y.Y. Gan, C.H. Liu, Y. Shi, Y.C. Zhao, S.Z. Kou, *Coatings*, 10 (2020) 73.
18. K.W. Kim, G.S. Ham, G.S. Cho, C.P. Kim, S.C. Park, K.A. Lee, *Intermetallics*, 130 (2021) 107061.
19. H. Zhang, Z.C. Yan, Q. Chen, Y. Feng, Z.G. Qi, H.Z. Liu, X.Y. Li, W.M. Wang, *J. Non-Cryst. Solids*, 564 (2021) 120830.
20. L. Zarazúa-Villalobos, N. Mary, J. Soo-Hyun, K. Ogawa, H. Kato, Y. Ichikawa, *J. Alloys Compd.*, 880 (2021) 160399.
21. J.E. Berger, A.M. Jorge, G.Y. Koga, V. Roche, C.S. Kiminami, C. Bolfarini, W.J. Botta, *Mater. Charac.*, 179 (2021).
22. P. Duwez, S.C.H. Lin, *J. Appl. Phys.*, 38 (1967) 4096.
23. T. Mizoguchi, K. Yamauchi, N. Niimura, *Jpn. J. Appl. Phys.*, 14 (1975) 711.
24. W.M. Yang, H.S. Liu, Y.C. Zhao, A. Inoue, K.M. Jiang, J.T. Huo, H.B. Ling, Q. Li, B.L. Shen, *Sci. Rep.*, 4 (2014) 1.
25. B. Sarac, Y.P. Ivanov, A. Chuvilin, T. Schöberl, M. Stoica, Z. Zhang, J. Eckert, *Nat. Commun.*, 9 (2018) 1333.
26. H. Fujimori, M. Kikuchi, Y. Obi, T. Masumoto, *Sci. Rep. Res. Inst. Tohoku Univ. Ser. A*, 26 (1976) 36.
27. E. Yüce, B. Sarac, S. Ketov, M. Reissner, J. Eckert, *J. Alloys Compd.*, 872 (2021) 159620.
28. J.L. Zhou, D.J. Kong, *J. Alloys Compd.*, 795 (2019) 416.
29. M.M. Vasić, T. Žák, N. Pizúrová, I.S. Simatović, D.M. Minić, *Metall. Mater. Trans, A*, 52 (2021) 34.
30. J.-C. Kang, S.B. Lalvani, C.A. Melendres, *J. Appl. Electrochem.*, 25 (1995) 376.
31. A. Lekatou, A. Marinou, P. Patsalas, M.A. Karakassides, *J. Alloys Compd.*, 483 (2009) 514.
32. Z.L. Long, C.T. Chang, Y.H. Ding, Y. Shao, P. Zhang, B.L. Shen, A. Inoue, *J. Non-Cryst. Solids*, 354 (2008) 4609.

33. G.Y. Koga, D. Travessa, G. Zepon, D.D. Coimbra, A.M. Jorge, J.E. Berger, V. Roche, J.C. Lepretre, C. Bolfarini, C.S. Kiminami, F. Wang, S.L. Zhu, A. Inoue, W.J. Botta, *J. Alloys Compd.*, 884 (2021) 161090.
34. H.G. Kim, M.S. Kim, W.N. Myung, *J. Korean Phys. Soc.*, 49 (2006) 1630.
35. F. Wang, A. Inoue, Y. Han, S.L. Zhu, F.L. Kong, E. Zanaeva, G.D. Liu, E. Shalaan, F. Al-Marzouki, A. Obaid, *J. Alloys Compd.*, 723 (2017) 376.
36. V.I. Tkatch, A.I. Limanovskii, S.N. Denisenko, S.G. Rassolov, *Mater. Sci. Eng., A*, 323 (2002) 91.
37. X.L. Jiang, Y. Li, M. He, L.X. Zhou, Q.J. Zheng, F.Y. Xie, W.J. Jie, D.M. Lin, *Int. J. Hydrogen Energy*, 44 (2019) 19986.
38. F.K. Yang, K. Sliozberg, I. Sinev, H. Antoni, A. Bähr, K. Ollegott, W. Xia, J. Masa, W. Grünert, B. Roldan Cuenya, W. Schuhmann, M. Muhler, *ChemSusChem*, 10 (2017) 156.
39. Y.J. Yue, Y.M. Zhu, F. Li, T. Xue, *Catal. Lett.*, 151 (2021) 507.
40. A. Bin Yousaf, M. Imran, M. Farooq, P. Kasak, *RSC Adv.*, 8 (2018) 3374.
41. J. Wu, T. Zhao, R. Zhang, R.K. Xu, J.K. Gao, J.M. Yao, Z. Anorg. *Allg. Chem*, 644 (2018) 1660.
42. R. Boppella, J. Tan, W. Yang, J. Moon, *Adv. Funct. Mater.*, 29 (2019) 1807976.
43. Y.M. Wang, D.D. Zhao, Y.Q. Zhao, C.L. Xu, H.L. Li, *RSC Adv.*, 2 (2012) 1074.
44. C.H. Hsu, F. Mansfeld, *Corrosion*, 57 (2001) 747.
45. B. Sarac, V. Zadorozhnyy, Y.P. Ivanov, A. Kvaratskheliya, S. Ketov, T. Karazehir, S. Gumrukcu, E. Berdonosova, M. Zadorozhnyy, M. Micusik, M. Omastova, A.S. Sarac, A.L. Greer, J. Eckert, *J. Power Sources*, 475 (2020) 228700.
46. Linear Polarization Resistance and Corrosion Rate - Theory and Background, in, Pine Research Instrumentation, 04/2016, pp. 1.
47. R.T. Loto, *Orient. J. Chem.*, 35 (2019) 1138.
48. K. Shahzad, M.H. Sliem, R.A. Shakoor, A.B. Radwan, R. Kahraman, M.A. Umer, U. Manzoor, A.M. Abdullah, *Sci. Rep.*, 10 (2020) 4314.
49. L. Onyeji, G. Kale, *J. Mater. Eng. Perform.*, 26 (2017) 5741.
50. Y.Y. Choi, M.H. Kim, *RSC Adv.*, 8 (2018) 30155.

© 2021 The Authors. Published by ESG (www.electrochemsci.org). This article is an open access article distributed under the terms and conditions of the Creative Commons Attribution license (<http://creativecommons.org/licenses/by/4.0/>).